JOURNAL OF SPACECRAFT AND ROCKETS
Vol. 45, No. 6, November–December 2008

Boundary-Layer Stability Calculations for the HIFiRE-1 Transition Experiment

Christopher R. Alba,* Heath B. Johnson,† Matthew D. Bartkowicz,‡ and Graham V. Candler§
University of Minnesota, Minneapolis, Minnesota 55455
and
Karen T. Berger¶
NASA Langley Research Center, Hampton Virginia 23681

DOI: 10.2514/1.37445

Boundary-layer stability analysis is performed by computational fluid dynamic simulation of experiments conducted in the National Aeronautics and Space Administration Langley Research Center 20-in. Mach 6 Air Tunnel in support of the first flight of the Hypersonic International Flight Research Experimentation program. From the laminar computational flow solutions, disturbances are calculated using the linear parabolized stability equations to obtain integrated disturbance growth rates. Comparisons are made between the experimentally observed transition locations and the results of the stability analysis. The stability results from the NASA Langley Research Center Air Tunnel are combined with previous work done for the Calspan University at Buffalo Research Center Large-Energy National Shock Tunnel to show excellent correlation between predicted and observed boundary-layer transition locations. Roughness calculations are also performed and a Reynolds number based on trip height is tabulated with experimental results.

Nomenclature

D	=	mass diffusion coefficient
E	=	disturbance kinetic energy, J
e^N	=	magnitude of disturbance amplification
H	=	enthalpy, J/kg
h	=	heat transfer coefficient, kg/m^2 · s
h_{ref}	=	reference coefficient using Fay–Riddell calculation to stagnation point of a sphere
k	=	trip height, m
L	=	reference geometry axial length, m
M	=	Mach number
N	=	natural logarithm of the total disturbance amplification
q	=	heat transfer rate, W/m^2
Re	=	unit Reynolds number, 1/m
Re_x	=	Reynolds number based on axial distance from nose
Re_θ	=	Reynolds number based on boundary-layer momentum thickness
s	=	surface distance, m
$s_\circ$	=	surface location of the first critical point, m
T	=	translational–rotational temperature, K
T_v	=	vibrational temperature, K
u'	=	complex fluctuating x-direction velocity component, m/s
v	=	velocity magnitude, m/s
v'	=	complex fluctuating y-direction velocity component, m/s
w'	=	complex fluctuating z-direction velocity component, m/s
x	=	axial distance from nose, m
y^+	=	first grid cell spacing relative to a viscous length scale
α	=	complex streamwise wave number, 1/m
δ	=	distance from the body surface to the boundary-layer edge, m
θ	=	boundary-layer momentum thickness, m
μ	=	dynamic viscosity, kg/m · s
ρ	=	density, kg/m^3
σ	=	disturbance growth rate, 1/m
ω	=	disturbance frequency, kHz

Subscripts

aw	=	adiabatic wall condition
e	=	local edge condition
eff	=	effective trip height condition
k	=	local trip height condition
tr	=	boundary-layer transition location condition
trip	=	trip location condition
w	=	wall condition
∞	=	freestream condition

Conventions

$\bar{r}$	=	mean value for any flow variable
r'	=	fluctuating component of any flow variable

Presented as Paper 505 at the 46th AIAA Aerospace Sciences Meeting and Exhibit, Reno, NV, 7–10 January 2008; received 7 March 2008; revision received 27 August 2008; accepted for publication 28 August 2008.

*2nd Lt., U.S. Air Force, Research Assistant, Department of Aerospace Engineering and Mechanics. Student Member AIAA.
†Senior Research Associate, Department of Aerospace Engineering and Mechanics. Senior Member AIAA.
‡Graduate Research Assistant, Department of Aerospace Engineering and Mechanics. Student Member AIAA.
§Professor, Department of Aerospace Engineering and Mechanics. Fellow AIAA.
¶Aerospace Engineer, Aerothermodynamics Branch. Member AIAA.

I. Introduction

AS CERTAIN classes of hypersonic cruise vehicles may spend significant amounts of time in conditions where the boundary layer is transitional, an accurate prediction of the boundary-layer transition location is a critical factor in determining the total heat load

on these vehicles. Because there is a large uncertainty in using algebraic methods such as Re_θ/M_e for estimating transition location [1], a more accurate approach based on the physics of the transition process must be applied. The parabolized stability equations (PSE) approach has been shown to provide reasonable predictions of boundary-layer transition locations for some geometries when coupled with semi-empirical correlations based on experimental measurements.

One of the goals of the Hypersonic International Flight Research Experimentation (HIFiRE) program is to provide high-quality data for boundary-layer stability analysis [2]. Previous comparisons of experimental and computational work for the HIFiRE program have been published [3–5], where heat transfer data from nine different Calspan University at Buffalo Research Center Large-Energy National Shock Tunnel (CUBRC LENS) experiments were used to compare the observed boundary-layer transition location with the results of PSE calculations for both sharp and blunt cones. In the current work, using the experimental data that have been collected in the NASA Langley Research Center (LaRC) 20-in. Mach 6 Air Tunnel, we continue a systematic comparison of stability calculations with experimental results.

II. Stability Analysis Using the e^N Method

The linearized parabolized stability equations used in this work are derived from the 2-D or axisymmetric Navier–Stokes equations by decomposing the instantaneous flow variables as a mean plus a fluctuating component, $r = \bar{r} + r'$, where r is any instantaneous flow variable.

The perturbation on the mean flow state is substituted into the Navier–Stokes equations and the mean flow solution is subtracted, resulting in the disturbance equations. All disturbances are assumed to be small such that nonlinear terms can be neglected. The disturbances are modeled as a fast-oscillatory wave part and a slowly varying shape function, and the solution of the PSE yields the spatial evolution of disturbances at a particular frequency in the boundary layer. More details about the PSE approach as implemented here can be found in Johnson and Candler [6].

A semi-empirical transition correlation that works well with the mechanism-based PSE approach is the e^N method in which N represents the streamwise-integrated growth rate of unstable boundary-layer disturbances at a fixed frequency:

$$N(\omega, s) = \int_{s_0}^{s} \sigma \, \mathrm{d}s \tag{1}$$

where $s_\circ$ is the location of the first critical point, and σ is the disturbance growth rate defined as

$$\sigma = -\mathrm{Im}(\alpha) + \frac{1}{2E}\frac{\mathrm{d}E}{\mathrm{d}s} \tag{2}$$

In this equation, $\mathrm{Im}(\alpha)$ is the imaginary part of the complex streamwise wave number and E is the disturbance kinetic energy defined as

$$E = \int_n \bar{\rho}(|u'|^2 + |v'|^2 + |w'|^2)\, \mathrm{d}n \tag{3}$$

where n is the direction normal to the body surface.

The PSE approach coupled with the e^N method has shown promising agreement with experiment [7]. Using the linear stability theory or the PSE to compute N factors for specific cases for which experimental data are available, the value of N at transition has been shown to be about 8–11 for the limited number of different smooth-body geometries in low-disturbance freestream conditions [8–10]. The influence of factors such as body roughness and higher levels of freestream noise are manifested in lower values of N, with values of around 5.5 showing good correlation with the onset of transition in noisier environments such as conventional wind tunnels or shock tunnels [4,11–13]. PSE calculations coupled with the e^N transition correlation using $N = 5.5$ have been found to work very well as a transition prediction criterion in previous work relating to the HIFiRE program [4].

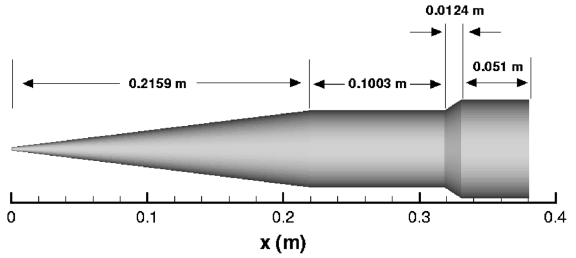

Fig. 1 Cone-cylinder-flare geometry with axial lengths denoted for each section.

III. Description of Experiments

Although the application of the linear stability theory together with the e^N transition correlation has been found to work fairly well for a variety of conditions, the accuracy of many e^N computations of high-speed flows remains uncertain. It is often not clear whether bluntness effects, wall temperature distributions, and so on were handled with sufficient accuracy [1]. To make a careful comparison with PSE calculations, detailed information about the geometry and flight conditions is required.

The experimental data presented here were generated from experiments conducted in the NASA LaRC 20-in. Mach 6 Air Tunnel. The experimentally measured wall heating rates were determined using LaRC's phosphor thermography system to obtain global heating images, which provide indication of the onset of boundary-layer transition [14]. The experiments tested five different body geometries. For the purposes of the computational fluid dynamics (CFD) simulations, the simpler geometries (blunt cones) were selected to run along with a few tests with more complex body geometries. All geometries have either a 1.19 or a 2.10-mm blunt nose radius. The simple blunt cones have an axial length of 0.381 m with a 7 deg half-angle. The more complex geometry has a shape described as a cone-cylinder flare (CCF), with a short flat section after the flare, which can be seen in Fig. 1. The nose has a radius of 1.19 mm. The conical section has a 7 deg half-angle which extends axially for 0.2159 m. The cylindrical section has a length of 0.1003 m. The flare has a half-angle of 33 deg with an axial length of 0.0124 m, and the final flat section has an axial length of 0.051 m for a total length of approximately 0.381 m.

A total of 22 runs with varying angles of attack and freestream unit Reynolds numbers were chosen for simulation. All of the simulations were run at Mach 6 with a 300 K isothermal wall. An isothermal 300 K wall was chosen because most of the phosphor thermography runs in the LaRC Air Tunnel have a 5–10 s duration, but the data are normally collected about 3 s into the run. For these tests, the model surface temperature increased anywhere from 10–80 K above room temperature (295 K), but usually was in the 20–40 K range. The adiabatic wall temperature at the nose is above 500 K for all of these runs. Hence, it is sensible to make an isothermal wall assumption. The freestream conditions for each run can be found in Table 1. Each run listed in Table 1 was simulated; however, we will not present results or analysis for runs 13, 25, 30, 60, and 61. The reasons for this will be discussed later in the paper but mainly dealt with the fact that we did not have a 3-D stability solver available to analyze the nonzero angle of attack (AoA) runs. See Berger et al. [15] for more details about the experiments.

IV. Mean Flow Solutions

All of the runs at 0-deg angle of attack used structured 2-D grids with 350×350 points for the blunt cones or 470×350 points for the CCF. The laminar mean flow solutions were generated using an optimized 2-D/axisymmetric mean flow solver based on the implicit data-parallel line relaxation (DPLR) method [16]. The solver

Table 1 Test conditions for the Mach 6 HIFiRE experiment simulations

Run	Model	AoA, deg	Re_∞, 1/m	ρ_∞, kg/m^3	T_∞, K	M_∞	Orientation
1	2.10 Cone	0	7.01×10^6	3.20×10^{-2}	62.56	5.97	——
4	1.19 Cone	0	6.97×10^6	3.19×10^{-2}	62.61	5.97	——
7	1.19 Cone	0	1.39×10^7	6.25×10^{-2}	62.05	6.01	——
8	1.19 Cone	0	1.92×10^7	8.77×10^{-2}	63.55	6.03	——
12	1.19 Cone	−3	1.39×10^7	6.29×10^{-2}	62.07	6.01	LW
13	1.19 Cone	−3	1.91×10^7	8.74×10^{-2}	63.53	6.03	LW
19	1.19 Cone	−5	1.36×10^7	6.14×10^{-2}	62.32	6.01	LW
24	1.19 Cone	3	1.38×10^7	6.26×10^{-2}	62.24	6.01	WW
25	1.19 Cone	3	1.92×10^7	8.79×10^{-2}	63.34	6.03	WW
29	1.19 Cone	5	1.39×10^7	6.27×10^{-2}	62.08	6.01	WW
30	1.19 Cone	5	1.94×10^7	8.82×10^{-2}	63.24	6.03	WW
36	CCF33	0	1.94×10^7	8.82×10^{-2}	63.12	6.03	——
37	CCF33	0	1.92×10^7	8.76×10^{-2}	63.52	6.03	——
39	CCF33	0	1.93×10^7	8.77×10^{-2}	63.16	6.03	——
58	2.10 Cone	0	1.94×10^7	8.83×10^{-2}	63.21	6.03	——
60	2.10 Cone	−5	1.92×10^7	8.77×10^{-2}	63.32	6.03	LW
61	2.10 Cone	5	1.93×10^7	8.79×10^{-2}	63.35	6.03	WW
62	1.19 Cone	0	1.94×10^7	8.81×10^{-2}	63.25	6.03	——
63	1.19 Cone	−3	1.94×10^7	8.84×10^{-2}	63.07	6.03	LW
64	1.19 Cone	−5	1.93×10^7	8.78×10^{-2}	63.29	6.03	LW
65	1.19 Cone	3	1.94×10^7	8.83×10^{-2}	63.07	6.03	WW
66	1.19 Cone	5	1.95×10^7	8.86×10^{-2}	63.09	6.03	WW

produces second-order accurate laminar flow solutions with low dissipation and shock capturing. The stability and transition analysis of hypersonic boundary-layers (STABL) suite includes functions for automatic grid tailoring based on the methods used in the NASA OUTBOUND code [17]. Grid tailoring was used for all runs at zero angle of attack to generate grids where the outer boundary closely followed the shock and the wall spacing met the desired criteria. Clustering of points was employed in regions where the flow exhibits large gradients and is strongly coupled in a particular direction, such as the wall–normal direction. To ensure that the boundary-layer solutions were well resolved, values of y^+ less than unity were obtained at the first solution point away from the wall.

The governing equations used in STABL are the Navier–Stokes equations extended for a gas mixture with ns species. A two-temperature model is used where the energy in the translational and rotational modes is characterized by the translational temperature T, and the energy of the vibrational modes is characterized by the vibrational temperature T_v. Closure of the governing Navier–Stokes equations is obtained through relations for the transport of mass, momentum, and thermal energy due to gradients of mass concentration, velocity, and vibrational and translational temperatures, respectively. The species diffusion velocity is given by Fick's law of mass diffusion. The mass diffusion coefficient D is found from assuming a constant Schmidt number of 0.5 which is the same for all species. For the 0-deg angle of attack runs chemistry and translational–vibrational energy exchange were included in the calculations. However, at the low freestream enthalpies simulated here, chemistry plays a negligible role in the results.

The laminar mean flow solutions for the runs at a nonzero angle of attack were generated using the unstructured 3-D implicit solver US3D which implements the DPLR and full matrix point relaxation methods [18,19]. The US3D flow solutions were modeled as perfect gas air. When analyzing the US3D mean flow solutions, PSE-Chem was also run as a perfect gas so that the gas model was consistent between solvers.

STABL's species viscosities are specified in a general fashion so that different viscosity models may be used through specified temperature ranges, and blending functions are used to maintain smooth function values and derivatives between models. The species translational conductivity is computed by Eucken's relation. The gas mixture viscosity and conductivity are found from the Wilke mixing law. The US3D mean flow solutions used the high temperature Blottner coefficients of nitrogen for the viscosity model. The viscosity model used for PSE-Chem was matched for either the STABL or the US3D flow solutions. More details about the models are available in Johnson and Candler [6] and Nompelis et al. [19].

V. PSE-Chem Analysis

The PSE-Chem solver used for these calculations solves the parabolized stability equations for supersonic and hypersonic applications, including effects of finite-rate chemistry and translational–vibrational energy exchange [6]. PSE-Chem is implemented using the message passing interface for efficient distribution of parallel calculations which were run on a Linux cluster. The STABL suite provides a graphical user interface and an object-oriented scripting interface to PSE-Chem to easily run all the cases that are required for a stability analysis. Because PSE-Chem is currently a 2-D/axisymmetric solver, a symmetry plane slice was taken from the 3-D mean flow solutions for stability analysis.

The automatic test matrix feature of PSE-Chem was used to set up the PSE analysis of each test case. A typical PSE analysis, illustrated in Fig. 2, uses between 2000–3000 test points where each point represents a unique combination of disturbance frequency and starting location. The PSE are solved in an identical fashion whether the resulting disturbances are characterized as first or second mode. The estimate of the first-mode disturbance frequency is obtained by taking one-tenth of the magnitude of the velocity at the boundary-layer edge over the distance from the surface to the boundary-layer edge ($V_e/10\delta$). The estimate of the second-mode disturbance

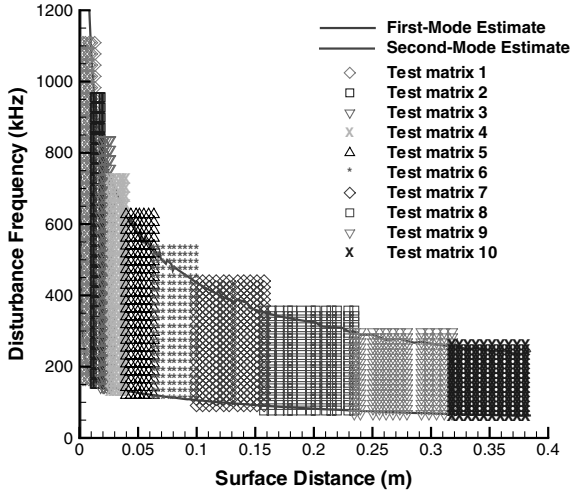

Fig. 2 PSE test matrices for run 4 using the automatic test matrix routine. Each test point represents a unique disturbance frequency and surface location for PSE analysis.

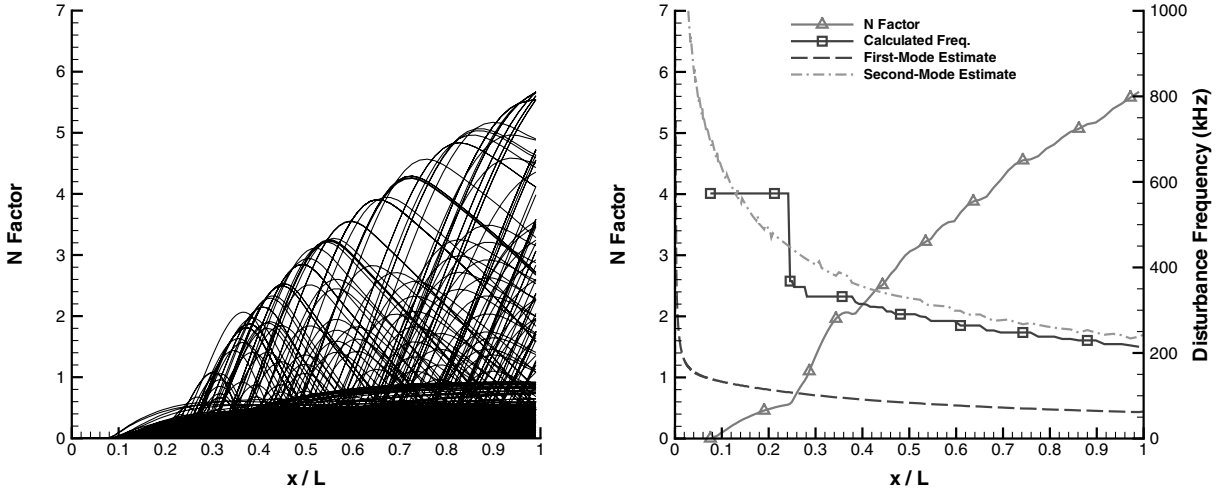

a) Raw PSE *N* factor results

b) Comparison of estimated and calculated most-unstable disturbance frequencies

Fig. 3 PSE results for blunt cone of run 4.

frequency is found by integrating the time it takes for a wave to travel from the surface to the relative Mach line in a boundary layer. Because it is known that first-mode disturbances are most unstable for oblique waves, and second-mode disturbances are most unstable for 2-D waves, we need to test our PSE results to determine which mode is dominant for a specific case. To accomplish this, the automatic test matrix routine covers both the estimated first- and second-mode disturbance frequencies with test points. If first-mode disturbances are found to be the most unstable, we then add test points for oblique waves.

The raw PSE results can be seen in Fig. 3a which shows *N* factor curves for each of the PSE test points. Each curve in the plot represents a disturbance at a given frequency where the starting location for the disturbance is varied to determine the upstream point resulting in the largest subsequent *N* factor. From the collected PSE *N* factors, we can extract the envelope of the maximum *N* factors and corresponding disturbance frequency that are reached at each surface location. Figure 3b shows typical PSE results indicating that the disturbances are second-mode dominant over a majority of the surface. Because all of these runs were found to be second-mode dominant, 2-D disturbances will only be of interest for this analysis.

VI. Analysis of Results

A. Predicted Transition Locations

A very small number of runs were tested in the wind tunnel at 0-deg angle of attack, and five of these runs were chosen for PSE analysis. The mean flow solutions for all of the 0-deg angle of attack runs were completed using the axisymmetric CFD solver provided in the STABL software suite, which was described in Sec. IV. Berger et al. [15] advised not to consider the lower freestream unit Reynolds number cases since either the transition was not observed or the wall heating was too low to measure reliably. Again, please refer to Table 1 for the freestream conditions of each run.

To evaluate whether a fixed value of *N* works well for estimating a transition location for these cases, we need to determine a transition location from the experimental results. Several methods exist for doing this. For example, in one commonly applied method, curves are fit through the laminar and transitional regions of the experimental data and a transition is deemed to occur at the intersection of these lines. Although this seems reasonable at first glance, in practice it requires a researcher to make judgments about which experimental data points to include in which curve fit, and by changing the collection of data points that are used, the determined transition location will move. Because it therefore ultimately falls to the judgment of the researcher to determine the transition location, we simply select a transition location by visual inspection of the experimental results. That is, we deem that transition has occurred where the experimental data appear to deviate significantly from the laminar trend. Although this leaves the precise values of some quantities open to different interpretations, it does not significantly affect the results or conclusions of this work.

The experimental runs chosen for simulation were 1, 4, 7, 8, and 58. Out of those selected runs, only runs 7 and 8 had definite experimentally observable transition locations. Although this may only provide limited data for comparing observed and predicted transition locations, it can also provide an important verification that PSE-Chem is getting maximum *N* factors which do not indicate transition for those runs exhibiting strictly laminar heating profiles.

The wind-tunnel tests use a nondimensional measure of the wall heat transfer defined as h/h_{ref}, where h is defined as [20]

$$h = q/(H_{\text{aw}} - H_w) \tag{4}$$

The value of h_{ref} is calculated using Fay–Riddell stagnation point heating of a sphere. The sphere used for this calculation had the same radius as each model's nose.

It was found that $N = 5.5$ correlated well with transition in the CUBRC LENS tunnels [4], and we should expect values around $N = 5.5$ to correlate with transition in this Mach 6 air tunnel because this is also another nonquiet tunnel. Figure 4 displays the maximum *N* factor curves for runs 1, 4, and 58, which were all blunt cones at 0-deg angle of attack. Although all of these runs had laminar heating profiles, only runs 4 and 58 achieved maximum *N* factors greater

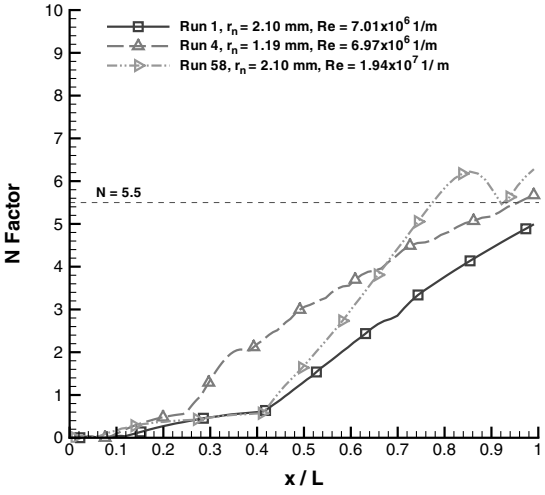

Fig. 4 Maximum *N* factors for runs 1, 4, and 58.

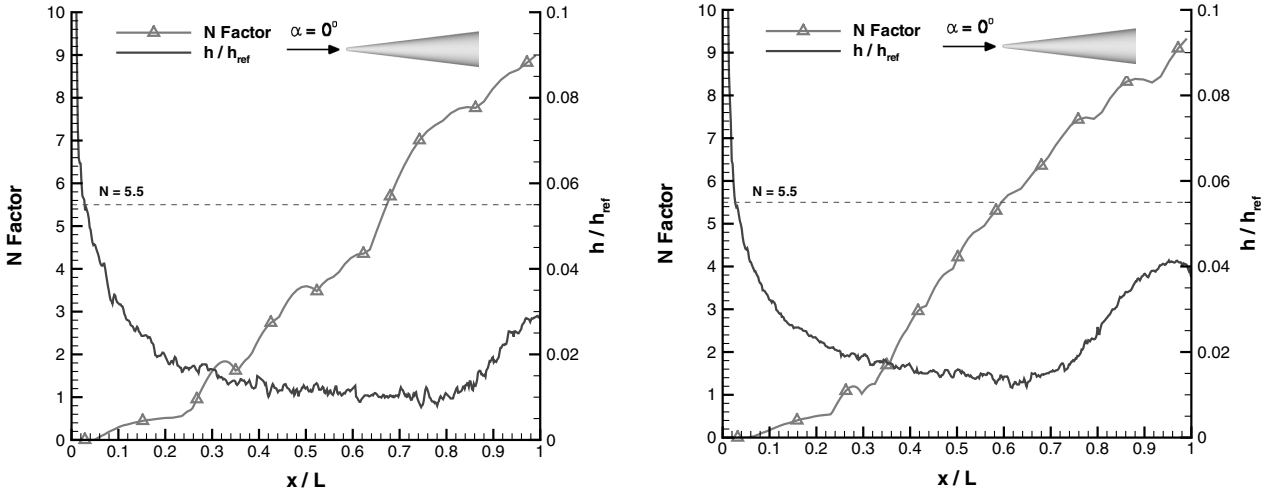

a) Run 7, $Re_\infty = 1.39 \times 10^7$ 1/m b) Run 8, $Re_\infty = 1.92 \times 10^7$ 1/m

Fig. 5 Maximum *N* factors and experimental wall heat rate for runs 7 and 8.

than 5.5. Run 4 reaches an N factor of 5.5 right at the end of the cone, which is consistent with the experimental result that transition was not observed. Run 58 reaches an N factor of 5.5 at approximately $x/L = 0.77$ and achieves a maximum N factor of approximately 6.2. This seems to be an instance where choosing $N = 5.5$ did not work well in correlating with boundary-layer transition. However, we will show that the actual N that correlates with transition for the LaRC tunnel is around 6–7.4. As a result, run 58 may be consistent with the collective stability results.

Figure 4 provides verification that our stability results are reflecting the differences in geometry and freestream conditions between the three runs with experimental laminar boundary layers. It is generally known that a small amount of nose bluntness has a stabilizing influence on boundary layers and delays the transition process. From this knowledge, the results are consistent with runs 1 and 58 having a larger nose bluntness than run 4 because the N factor growth was delayed over a larger portion of the body. The slopes of the N factor curves are also consistent with each run's freestream unit Reynolds number. Run 58 had the highest freestream unit Reynolds number and has the corresponding largest slope for its N factor curve; whereas, run 4 had the lowest freestream unit Reynolds number and the slope for its N factor curve reflects this.

The only two simulations for which the corresponding experiments clearly indicated transition were runs 7 and 8, which were 1.19 mm blunt cones. Although these two runs had the same geometry, the freestream unit Reynolds number was increased from 1.39×10^7 (1/m) to 1.92×10^7 (1/m). Figure 5 shows the maximum N factors along with the experimental wall heat transfer rate for runs 7 and 8. There is a line drawn at $N = 5.5$ to show how the predicted transition x/L locations for the calculated results compare against the experiments. To better illustrate this, we choose a transition value of $N = 5.5$ and plot predicted versus observed transition Reynolds numbers for each run. The results for runs 7 and 8 from the LaRC wind tunnel are combined with the CUBRC LENS tunnel results [4], shown in Fig. 6, which displays how $N = 5.5$ correlates with transition across two different facilities. If the predicted and observed transition locations agree, the data points should fall along a straight line. For these LaRC runs, a fixed value of $N = 5.5$ correlates the observed transition location fairly well and, overall, there is excellent agreement between the observed and predicted transition locations. This correlated data shown in Fig. 6 span a range of freestream Mach numbers, unit Reynolds numbers, enthalpies, and nose bluntness.

We can see from Fig. 5 that experimental transition occurs at a larger N factor than 5.5 for both runs. For run 7, experimental transition occurs approximately at $x/L = 0.78$ where $N = 7.4$ and the disturbance frequency is 333 kHz. For run 8, experimental transition occurs approximately at $x/L = 0.65$ where $N = 6.0$ and

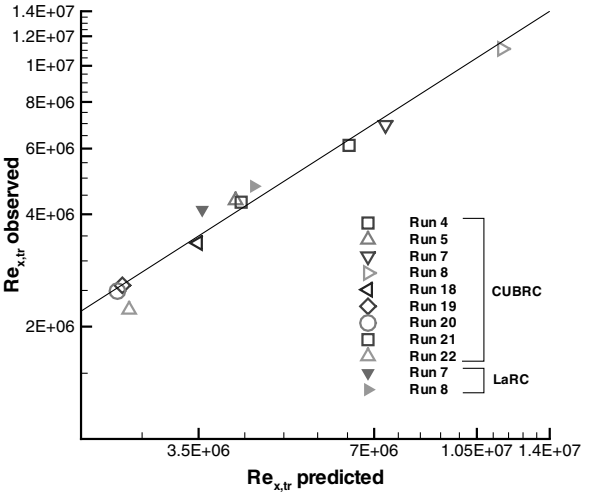

Fig. 6 Comparison of predicted and observed transition Reynolds numbers using the correlation $N = 5.5$.

the disturbance frequency is 430 kHz. The higher frequency is a result of second-mode disturbances being tuned to boundary-layer thickness and the higher freestream Reynolds number in run 8. As discussed previously, determination of the experimental x/L transition location is imprecise and one could choose a range of locations arguably signifying transition onset. In addition, there was some uncertainty in the experimental wall heating rate measurement between runs which had approximately identical freestream conditions and body geometry (shown in Fig. 10), which augments the amount of uncertainty in determining the experimental transition location. Using $N = 5.5$ as an approximation for predicting boundary-layer transition seems to work well for nonquiet tunnels, but the actual N factor at transition will vary due to the accuracy of experimental measurements and differences in freestream noise levels between conventional tunnels [21].

For the experiments at a nonzero angle of attack, PSE analysis was completed on symmetry plane slices taken from the full 3-D mean flow solution. Because we do not have a 3-D stability solver available, the symmetry planes were the only logical place to apply a 2-D solver. Our analysis investigates the limits of applying 2-D solvers to symmetry planes of 3-D flows. The PSE-Chem solver can be run either as axisymmetric or 2-D, but because the 3-D mean flow for a nonzero angle of attack run is not axisymmetric, the stability analysis on the symmetry plane was performed as a 2-D problem. The 3-D mean flow solutions for all of the nonzero angle of attack

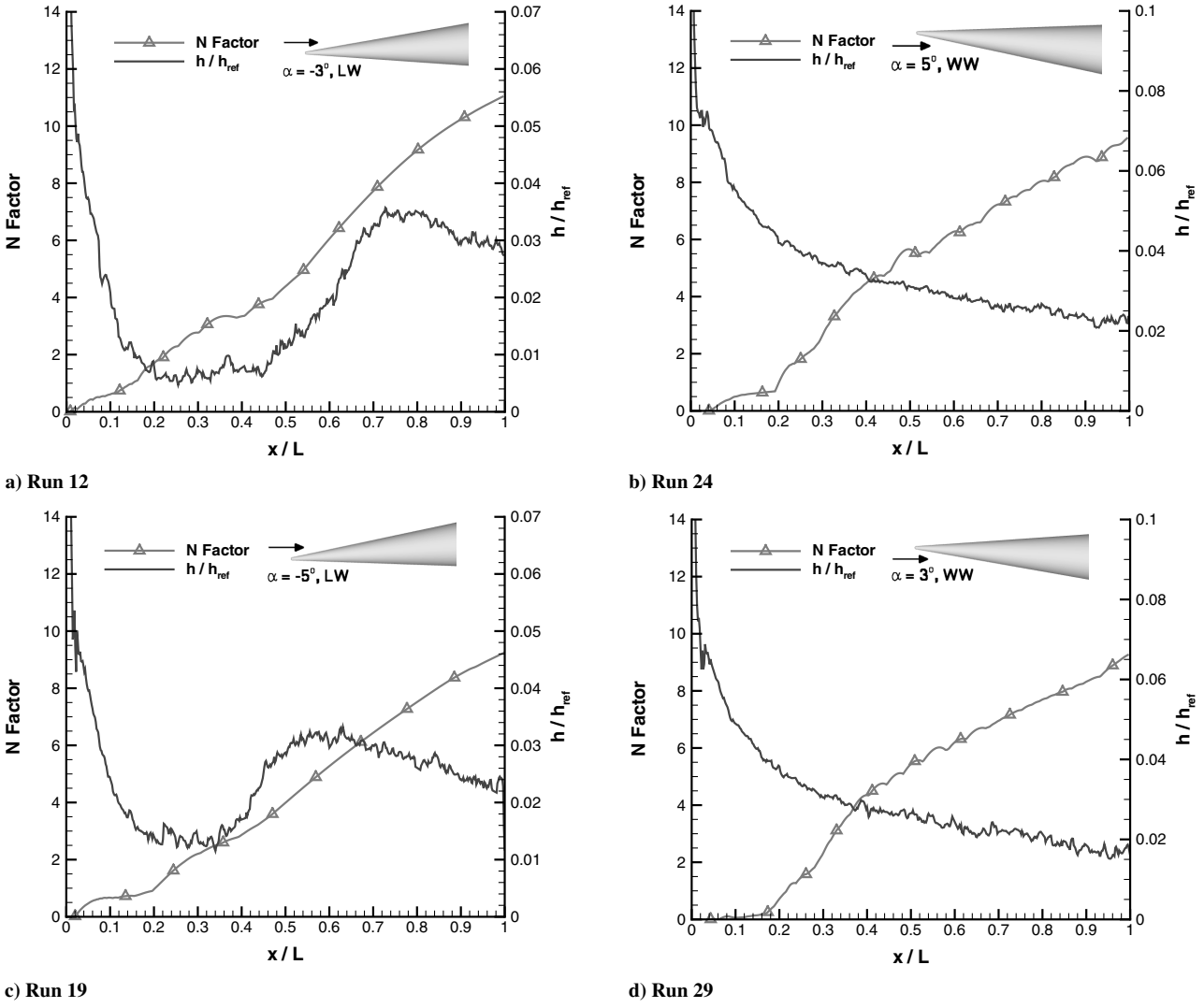

a) Run 12 b) Run 24

c) Run 19 d) Run 29

Fig. 7 Maximum *N* factors and experimental wall heat rate for runs 12, 19, 24, and 29.

runs were completed using the CFD solver US3D, which was described in Sec. IV. The maximum *N* factor and experimental wall heat transfer rate for runs 12, 19, 24, and 29 are shown in Fig. 7. All these runs were 1.19 mm blunt cones at a freestream unit Reynolds number of approximately 1.4×10^7 1/m. For runs 12 and 19, the experimental results show transition to occur earlier than what would be predicted if an *N* factor of 5.5 was chosen. Experimental transition is observed when the *N* factor is approximately 3.8 for run 12 and 2.5 for run 19. For runs 24 and 29, it is clear that the flow was completely laminar for the experimental tests while a maximum *N* factor of almost 10 was achieved for both runs. Using $N = 5.5$ as a transition prediction correlation does not work here, and it is not clear what mechanism is causing transition for these cases, although it is suspected that three-dimensional and cross-flow effects play a large role. The rest of the nonzero angle of attack runs, specifically runs 13, 25, 30, 60, and 61, displayed similar unreliable stability results using our current methods.

It is important to consider the 3-D mean flow characteristics near both symmetry planes where the mean flow direction is not just along the centerline. Figure 8 shows selected streamlines near the surface for the 1.19 mm blunt cone of run 13. This run is at an angle of attack of 3 deg and a 5-deg angle of attack case will have similar looking streamlines. Because of the conical shape of the body geometry, the flow gets turned toward the symmetry plane on the leeward (LW) side and away from the symmetry plane on the windward (WW) side. The deflection is made larger within the boundary layer because there is lower momentum fluid near the wall. This develops a velocity component inside the boundary layer that is perpendicular to the local inviscid-flow velocity vector, which is called crossflow. The crossflow profile exhibits an inflection point and causes crossflow vortex structures to form [22]. Velocity profiles with inflection points are an inherently unstable condition which may cause boundary-layer transition. Even though there is no crossflow component along the leeward and windward symmetry planes, the flow is clearly changed by the 3-D flow characteristics and differs from what would

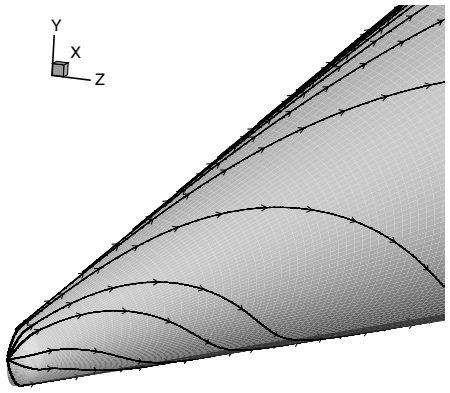

Fig. 8 Selected streamlines for run 13 with the top side being windward.

Table 2 Trip and run conditions for each simulated tripped run

Run	Trip height, k, m	Trip location, x/L	$(x/L)_{tr}$	AoA, deg	Orientation
36	1.65×10^{-4}	0.1114	0.28	0	——
37	2.92×10^{-4}	0.1114	0.23	0	——
39	1.143×10^{-4}	0.1114	-	0	——
62	2.92×10^{-4}	0.18	0.27	0	——
63	2.92×10^{-4}	0.18	0.37	−3	LW
64	2.92×10^{-4}	0.18	0.30	−5	LW
65	2.92×10^{-4}	0.18	0.25	3	WW
66	2.92×10^{-4}	0.18	0.24	5	WW

be obtained in a purely 2-D flow. Hence, there is no reason to attempt any kind of correlation for the nonzero angle of attack runs because PSE-Chem does not currently model all of the physical mechanisms for a 3-D flow.

B. Roughness Correlations

A certain number of tests were run specifically to observe how transition was affected by different discrete roughness element trip heights and locations. Table 2 lists the trip parameters, approximate transition location, angle of attack, and orientation of each tripped run which was simulated. All listed runs have the same approximate freestream unit Reynolds number of 1.9×10^7 (1/m). The experimentally measured wall heat transfer rate and heating images were used to determine the effectiveness of the trip in promoting boundary-layer transition.

To illustrate the effectiveness of a trip, refer to Fig. 9a where boundary-layer profiles at the x/L location of the trip are shown with the trip height for runs 63 and 65. The trip was placed at $x/L = 0.18$ for both runs. Figure 9a demonstrates that the thickness of the boundary layers is quite different for these two runs. Run 63 has a very thick boundary layer and the trip height is approximately 10% of the boundary-layer thickness. Run 65 has a much thinner boundary layer and the trip height is approximately 70% of the boundary-layer thickness. Figure 9b shows the measured wall heat transfer rate from which we can determine if the boundary layer actually transitioned due to the presence of the trip. Runs 63 and 65 have the same body geometry, freestream conditions, trip height, and trip location. However, run 63 considers the leeward side of the cone, whereas run 65 considers the windward side of the cone. Comparing the heating rates in Fig. 9b, it appears that run 63 transitions naturally with a small spike at the trip location, but overall the boundary layer for this run is unaffected by the trip. On the other hand, run 65 has a pronounced spike in its heating rate at the trip location, and the boundary layer begins to transition almost immediately. Run 13 did not use trips and essentially has the same freestream conditions as run 63, along with the same geometry, angle of attack, and orientation.

Hence, the experimentally measured wall heating rate of run 13 can be compared to run 63, which will allow us to determine if transition occurs earlier on the cone due to the trip. Figure 10 plots the experimental wall heating rates for runs 13 and 63 which shows that transition occurs approximately over the same area of the cone for both runs. However, this is not entirely conclusive as run 13 appears to transition sooner than run 63, which is an interesting observation because run 13 was not tripped. Small amounts of roughness delaying transition have been reported by Holloway and Sterrett [23], but the mechanism for the delay was unknown. The reason for the small differences in the experimental wall heating rates seen in Fig. 10 remains unknown.

A Reynolds number based on trip height, which uses the local flow conditions at the trip height, may be used to correlate surface roughness with boundary-layer transition. This has been termed the critical roughness Reynolds number which is defined as an effective trip height that causes an abrupt breakdown to turbulence [24]. However, for this paper we will calculate roughness Reynolds numbers Re_k and determine if the trip can be deemed effective. The roughness Reynolds number is defined as

$$Re_k = \frac{\rho_k v_k k}{\mu_k} \tag{5}$$

where all quantities are measured at the trip height, k. Table 3 tabulates Re_k values along with boundary-layer edge quantities measured at the trip and estimated experimental transition locations for the runs that were tripped. The quantities $(M_e)_{trip}$ and $(Re_{x,e})_{trip}$ are the calculated edge Mach number and local edge Reynolds number based axial distance from the nose at the trip location, respectively. The quantities $(\rho_e u_e k/\mu_e)_{tr}$ and $(Re_\theta/M_e)_{tr}$ are the calculated roughness Reynolds number based on local edge conditions and the Reynolds number based on the boundary-layer

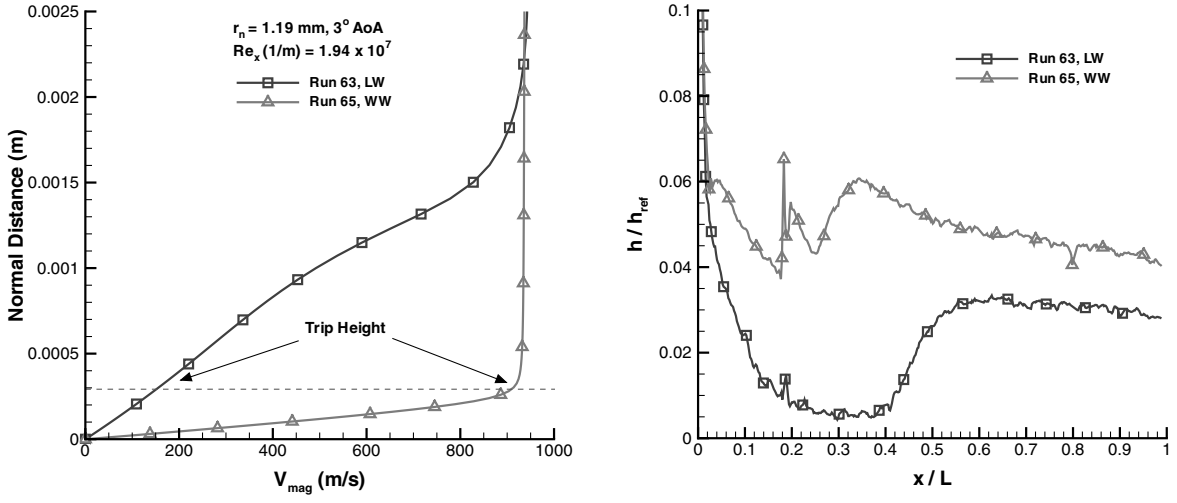

a) Boundary-layer profiles **b) Experimental wall heating profiles**

Fig. 9 Comparison of boundary-layer and experimental wall heating profiles for runs 63 and 65.

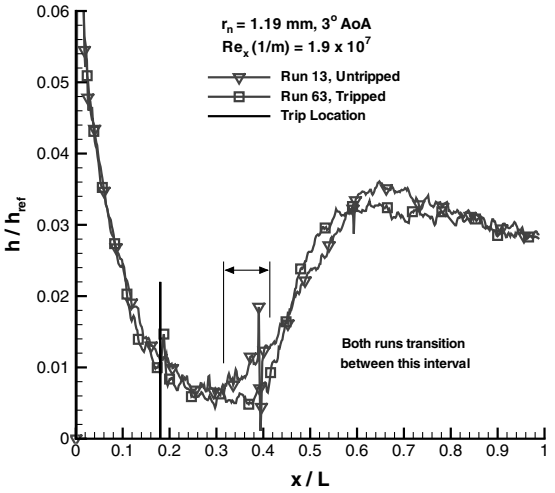

Fig. 10 Experimentally measured leeward wall heating profiles for runs 13 and 63.

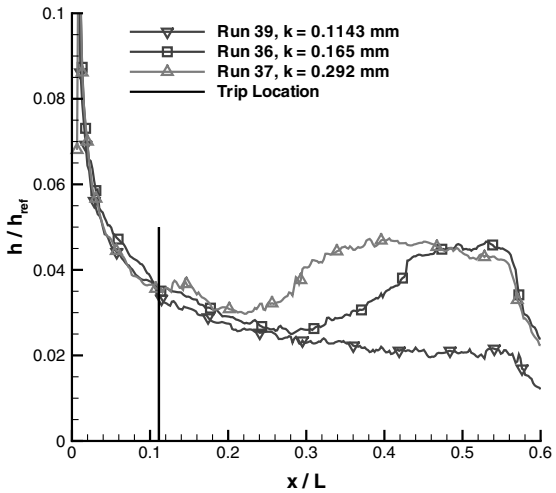

Fig. 11 Experimentally measured wall heat rates for runs 36, 37, and 39.

momentum thickness over edge Mach number at the transition location, respectively. The last column of Table 3 indicates whether the run had an effective trip height. Two of the runs, 39 and 63, did not produce boundary-layer transition as a result of the presence of a trip, as shown in Figs. 10 and 11. These two runs had the lowest Re_k values out of all the tripped runs. The one parameter that could not be determined from the experimental data was the critical roughness Reynolds number. The experimental tripped runs shown in this paper do not systematically increase the trip height or freestream Reynolds number until transition is first observed immediately following the trip location.

There is also the possibility of using these data in an attempt to correlate trip height with boundary-layer edge quantities to determine if transition would occur. The $(M_e)_{\text{trip}}$ and $(Re_{x,e})_{\text{trip}}$ values remain relatively constant while the Re_k value changes by a factor of almost 10 when comparing runs 36, 37, and 39. All three of these runs were 1.19-mm blunt nose CCF geometries at approximately $Re_\infty = 1.9 \times 10^7$ 1/m. The experimental wall heating rates for these three runs are plotted in Fig. 11, which displays how the increasing trip height affects the transition location. It is also important to note that none of the trips used reached an effective height for these three runs. Nevertheless, this seems to suggest that a certain critical Re_k value could correlate to transition for these simulated runs. Table 4 presents the data sorted by whether the boundary layer transitioned due to the presence of the trip, although not necessarily immediately following the trip, which shows increasing Re_k values until transition is observed. Table 4 shows that trips placed at a boundary-layer location giving a Re_k value less than 60 would not transition, whereas a value greater than 100 would transition. There is a large gap in the Re_k value between runs 37 and 65 which makes it difficult to estimate, or even interpolate, a critical roughness Reynolds number.

Reda [24] and Berry and Horvath [20] use a generalized approach for the development of boundary-layer transition correlation to surface roughness. This approach tries to establish empirical correlations using relevant similarity parameters for the transition process with experimental data. Correlations are investigated by comparing boundary-layer properties at the roughness location to some measure of roughness. The objective is to determine a critical roughness Reynolds number that correlates with boundary-layer transition in hypersonic flows. An ideal correlation is obtained when the results, plotted in log–log coordinates, fall along a straight line with a 45 deg slope ($n = -1$ power-law curve fit). This ideal situation allows the use of an algebraically simple relation to predict the effect of roughness on transition using easily computed boundary-layer parameters. However, this approach works best with data obtained from effective trip heights. Out of the eight tripped runs simulated, only runs 65 and 66 could be deemed effective trip heights because transition was observed immediately following the trip location. Two data points do not provide sufficient reason to attempt any kind of boundary-layer transition to surface roughness correlation.

VII. Conclusions

The results presented in this paper used experimental wall heat transfer data from the NASA Langley Research Center 20-in. Mach 6 Air Tunnel to compare the observed boundary-layer transition

Table 4 Tripped runs sorted by whether they transitioned due to the trip

Run	Transition?	k_{eff}?	Re_k
39	No	No	53.084
63	No	No	58.053
64	Yes	No	97.262
36	Yes	No	115.294
62	Yes	No	412.269
37	Yes	Yes	500.575
65	Yes	Yes	4508.060
66	Yes	Yes	7454.760

Table 3 Roughness correlation quantities for each simulated tripped run

Run	Re_k	$(M_e)_{\text{trip}}$	$(Re_{x,e})_{\text{trip}}$	$(\rho_e u_e k/\mu_e)_{\text{tr}}$	$(Re_\theta/M_e)_{\text{tr}}$	Orien.	k_{eff}?
36	115.294	3.102	1.678×10^5	1.027×10^3	77.854	——	No
37	500.575	3.142	1.720×10^5	1.706×10^3	71.102	——	No
39	53.084	3.140	1.723×10^5	——	——	——	No
62	412.269	3.345	3.461×10^5	1.740×10^3	75.451	——	No
63	58.053	3.525	3.182×10^5	——	——	LW	No
64	97.262	3.863	3.568×10^5	2.187×10^3	547.300	LW	No
65	4508.060	4.594	1.346×10^6	6.745×10^3	88.474	WW	Yes
66	7454.760	4.633	1.710×10^6	7.643×10^3	85.790	WW	Yes

location with the results of PSE calculations on blunt cones. Using the STABL suite and US3D, we were able to generate high-quality CFD mean flow and PSE solutions. The PSE method coupled with the semi-empirical e^N transition correlation using approximately $N = 5.5$ was found to work fairly well in all of the 0-deg angle of attack cases. Agreement between observed and predicted transition locations was reasonable for the 0-deg angle of attack cases with the blunt cone geometries having two different values of nose bluntness. The PSE calculations were also in agreement with the runs that exhibited laminar boundary layers because the N factor remained below or just reaching approximately 5.5. Combining the stability results from the LaRC and CUBRC LENS facilities, and using $N = 5.5$ as an approximate transition correlation, provides a good verification that the PSE approach coupled with the e^N method gives reasonable results in predicting boundary-layer transition locations over varying geometries and freestream conditions.

The three-dimensional flows calculated for runs at a nonzero angle of attack were found not to correlate well with an $N = 5.5$ predicted transition location with the current calculations, and it is not clear what mechanism was causing transition. Performing a 2-D stability analysis on a symmetry plane slice of a 3-D mean flow solution proved not to be practical in this case, and the nonzero angle of attack runs require further analysis before definite conclusions can be drawn. This further emphasizes the need for a three-dimensional boundary-layer stability solver that accounts for these three-dimensional effects to test whether a more accurate prediction of the transition location can be obtained.

Roughness data were also tabulated to help understand the role surface roughness plays in the boundary-layer transition process. Reynolds numbers based on trip height (Re_k) were calculated in an attempt to correlate surface roughness with boundary-layer transition. It appeared that runs with nearly identical freestream unit Reynolds numbers (36, 37, and 39) had boundary-layer edge quantities, which were measured at the trip location, that remained unchanged whereas Re_k values differed by a factor of almost 10. It is hoped that these data can be extended by other researchers to continue to build better roughness/boundary-layer transition correlations.

Acknowledgments

HIFiRE is a joint program of the U.S. Air Force Research Laboratory and the Australian Defence Science Technology Organisation (DSTO). The U.S. portion of the technical program is managed by the U.S. Air Force Research Laboratory Air Vehicles Directorate RBAA. This work was sponsored by Sandia National Laboratories Award no. 619327 and by the U.S. Air Force Office of Scientific Research under grant no. FA9550-04-1-0341. The views and conclusions contained herein are those of the authors and should not be interpreted as necessarily representing the official policies or endorsements, either expressed or implied, of the U.S. Air Force Office of Scientific Research, or the U.S. Government.

References

[1] Schneider, S. P., "Flight Data for Boundary-Layer Transition at Hypersonic and Supersonic Speeds," *Journal of Spacecraft and Rockets*, Vol. 36, No. 1, 1999, pp. 8–20. doi:10.2514/2.3428

[2] Dolvin, D., "Hypersonic International Flight Research and Experimentation (HIFiRE) Fundamental Sciences and Technology Development Strategy," AIAA Paper 2008-2581, May 2008.

[3] MacLean, M., Mundy, E., Wadhams, T., Holden, M., Johnson, H., and Candler, G., "Comparisons of Transition Prediction Using PSE-Chem to Measurements for a Shock Tunnel Environment," AIAA Paper 2007-4490, June 2007.

[4] Johnson, H., Alba, C., Candler, G., MacLean, M., Wadhams, T., and Holden, M., "Boundary-Layer Stability Analysis of the Hypersonic International Flight Research Transition Experiments," *Journal of Spacecraft and Rockets*, Vol. 45, No. 2, March 2008, pp. 228–236. doi:10.2514/1.31878

[5] MacLean, M., Wadhams, T., Holden, M., and Johnson, H., "A Computational Analysis of Ground Test Studies of the HIFiRE-1 Transition Experiment," AIAA Paper 2008-641, Jan. 2008.

[6] Johnson, H. B., and Candler, G. V., "Hypersonic Boundary Layer Stability Analysis Using PSE-Chem," AIAA Paper 2005-5023, June 2005.

[7] Reshotko, E., "Boundary Layer Instability, Transition, and Control," AIAA Paper 94-0001, Jan. 1994.

[8] Jaffe, N. A., Okamura, T. T., and Smith, A. M. O., "Determination of Spatial Amplification Factors and Their Application to Predicting Transition," *AIAA Journal*, Vol. 8, No. 2, Feb. 1970, pp. 301–308. doi:10.2514/3.5660

[9] Chen, F. J., Malik, M. R., and Beckwith, I. E., "Boundary-Layer Transition on a Cone and Flat Plate at Mach 3.5," *AIAA Journal*, Vol. 27, No. 6, June 1989, pp. 687–693. doi:10.2514/3.10166

[10] Malik, M. R., "Hypersonic Flight Transition Data Analysis Using Parabolized Stability Equations with Chemistry Effects," *Journal of Spacecraft and Rockets*, Vol. 40, No. 3, May–June 2003, pp. 332–344. doi:10.2514/2.3968

[11] Malik, M., Spall, R., and Chang, C.-L., "Effect of Nose Bluntness on Boundary Layer Stability and Transition," AIAA Paper 90-0112, Jan. 1990.

[12] Stilla, J., "Engineering Transition Prediction for a Hypersonic Axisymmetric Boundary Layer," *Journal of Aircraft*, Vol. 31, No. 6, Nov. 1994, pp. 1358–1364. doi:10.2514/3.46659

[13] Johnson, H. B., Seipp, T. G., and Candler, G. V., "Numerical Study of Hypersonic Reacting Boundary Layer Transition on Cones," *Physics of Fluids*, Vol. 10, No. 10, Oct. 1998, pp. 2676–2685. doi:10.1063/1.869781

[14] Merski, N. R., "Reduction and Analysis of Phosphor Thermography Data with the IHEAT Software Package," AIAA Paper 98-0712, 1998.

[15] Berger, K. T., Greene, F. A., and Kimmel, R. L., "Aerothermodynamic Testing and Boundary Layer Trip Sizing of the HIFiRE Flight 1 Vehicle," AIAA Paper 2008-0640, Jan. 2008.

[16] Wright, M. J., Candler, G. V., and Bose, D., "A Data-Parallel Line-Relaxation Method for the Navier-Stokes Equations," AIAA Paper 97-2046CP, June 1997.

[17] Saunders, D., Yoon, S., and Wright, M., "An Approach to Shock Envelope Grid Tailoring and Its Effect on Reentry Vehicle Solutions," AIAA Paper 2007-207, Jan. 2007.

[18] Nompelis, I., Drayna, T. W., and Candler, G. V., "Development of a Hybrid Unstructured Implicit Solver for the Simulation of Reacting Flows Over Complex Geometries," AIAA Paper 2004-2227, 2004.

[19] Nompelis, I., Drayna, T. W., and Candler, G. V., "A Parallel Unstructured Implicit Solver for Hypersonic Reacting Flow Simulation," AIAA Paper 2005-4867, June 2005.

[20] Berry, S. A., and Horvath, T. J., "Discrete Roughness Transition for Hypersonic Flight Vehicles," AIAA Paper 2007-307, Jan. 2007.

[21] Schneider, S. P., "Effects of Roughness on Hypersonic Boundary-Layer Transition," AIAA Paper 2007-0305, Jan. 2007.

[22] Balakumar, P., and Reed, H. L., "Stability of Three-Dimensional Supersonic Boundary Layers," *Physics of Fluids A*, Vol. 3, No. 4, April 1991, pp. 617–632. doi:10.1063/1.858123

[23] Holloway, P. F., and Sterrett, J. R., "Effect of Controlled Surface Roughness on Boundary-Layer Transition and Heat Transfer at Mach Numbers of 4.8 and 6.0," NASA TN-D-2054, April 1964.

[24] Reda, D. C., "Review and Synthesis of Roughness-Dominated Transition Correlations for Reentry Applications," *Journal of Spacecraft and Rockets*, Vol. 39, No. 2, March–April 2002, pp. 161–167. doi:10.2514/2.3803

R. Kimmel
Associate Editor